Supporting Information

Catalysis of Cu Cluster for NO Reduction by CO: Theoretical Insight into the Reaction Mechanism

Nozomi Takagi,[1] Kazuya Ishimura,[2] Hiroki Miura,[1,3] Tetsuya Shishido,[1,3] Ryoichi Fukuda,[1] Masahiro Ehara,[1,2]* and Shigeyoshi Sakaki[1,4]*

[1] Elements Strategy Initiative for Catalysts and Batteries, Kyoto University, 1-30 Goryo-Ohara, Nishikyo-ku, Kyoto 615-8245, Japan

[2] Institute for Molecular Science, Okazaki 444-8585, Japan

[3] Department of Applied Chemistry, Graduate School of Urban Environmental Sciences, Tokyo Metropolitan University, 1-1, Minami-osawa, Hachioji, Tokyo 192-0397, Japan

[4] Fukui Institute for Fundamental Chemistry, Kyoto University, 34-4 Takano-Nishihiraki-cho, Sakyo-ku, Kyoto 606-8103, Japan

Table of Contents:

1. Optimized Structures and Relative Energies of NO, NO - CO, and NO - NO Adsorbed Structures on Cu_{38}

As the initial step of the NO reduction by CO, we investigated adsorption positions of the Cu_{38} surface for NO and CO molecules, as shown in Figure S1.

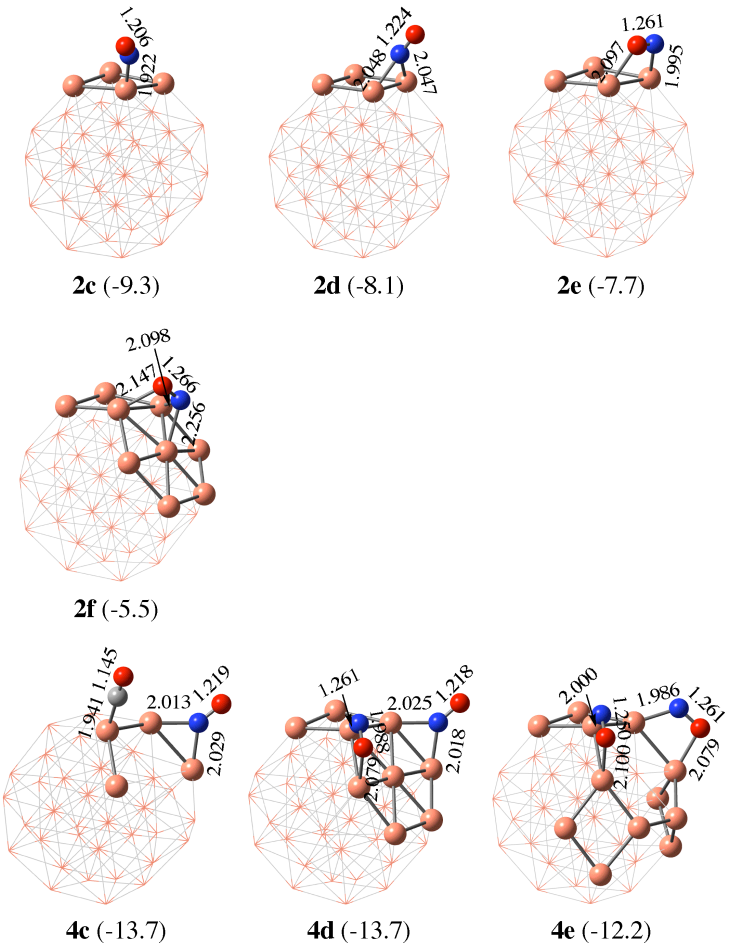

Figure S1. Optimized structures and relative energies of NO, NO - CO, and NO - NO adsorbed structures on Cu_{38}. In parentheses are the Gibbs energy change relative to Cu_{38} + 2 NO + CO. Distances and energies are in angstrom and kcal/mol, respectively.

2.1. NO Dissociative Adsorption on Cu_{38} and Size Effect of Cu Cluster

In one of the plausible mechanisms, NO reduction by CO with transition-metal catalyst starts to occur by dissociative NO adsorption. We investigated the energy change by elongating the N−O distance in **2b**, where the geometry was optimized at each N−O distance as shown in Figure S2a.

2.2. Size Effect of Cu Cluster

Cu_{38} is not general but smaller than a real catalyst, as will be described in the section of models. Thus, size effects of Cu particles on NO-CO reaction must be investigated in the near future. Preliminary computational results show moderate size effects on NO dimerization by the Cu nanoclusters as shown in Figure S2b, c. The DFT calculation with PBE functional under periodic boundary condition suggests that the NO dimerization on Cu_{38} occurs with no barrier. This result is not surprising because the GGA-type functional tends to underestimate the activation barrier. The same calculation showed that the NO dimerization occurred with marginal activation barrier of only 1.8 kcal/mol by Cu_{55}. The reaction energy by Cu_{38} is more negative than that by Cu_{55} but the difference is not very large. These results suggest that Cu_{55} is also reactive for NO dimerization like Cu_{38}. However, further theoretical study is needed to investigate size effects on NO dimerization and other elementary steps using different size of Cu nanoparticle.

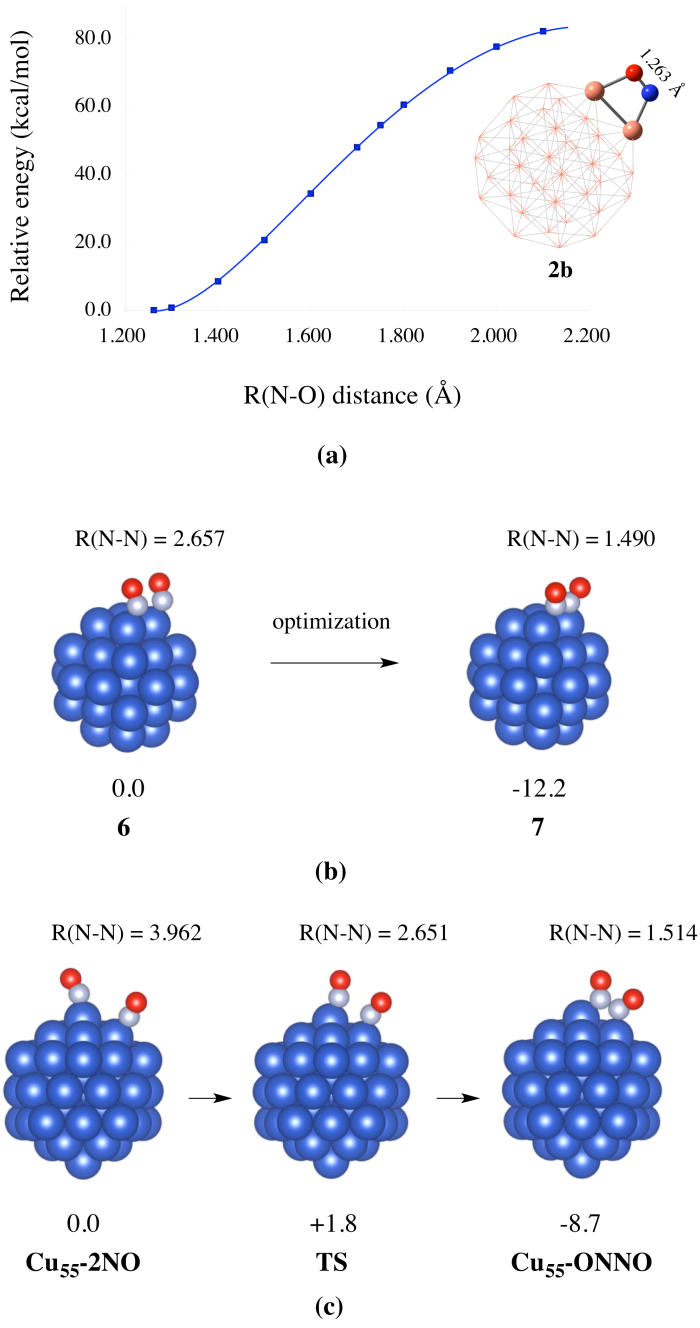

Figure S2. (a) Potential energy curve for dissociative NO adsorption on Cu_{38}. (b) Geometry optimization of **6**[a] leads to the NO dimer structure **7** by DFT calculation with plane wave basis sets using PBE functional.[b] (c) Geometry and energy change for NO dimerization on Cu_{55} cluster by DFT calculation with plane wave basis sets using PBE functional.[b] Energy and distances are in kcal/mol and angstrom, respectively.

[a] Geometry optimization started from the B3LYP-optimized geometry.

[b] The DFT calculations using PBE functional[S1] and plane wave basis sets were carried out with the VASP program package.[S2-S4] Plane wave basis sets were employed with an energy cutoff 400 eV. The Monkhorst-Pack grid method was used for $1 \times 1 \times 1$ *k*-point sampling. The compounds were placed at the center of a $25 \times 25 \times 25$ Å cubic box with periodic boundary condition, which was enough to neglect the interaction between a compound and its periodic image. Convergence criteria for total energy and maximum force were set to 1.0×10^{-4} eV and 0.01 eV/Å, respectively.

3. Optimized Geometry of Other Plausible Intermediates and Pathways

Plausible intermediates and pathways investigated in this work are shown below (Figure S3 - S8).

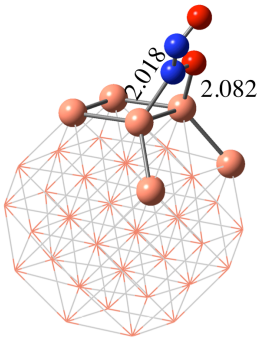

24 (+9.1)

Figure S3. Optimized geometry of a plausible intermediate for another ONNO flapping on the same Cu atoms. In parenthesis is the energy change relative to **7**. Distances and energies are in angstrom and kcal/mol, respectively.

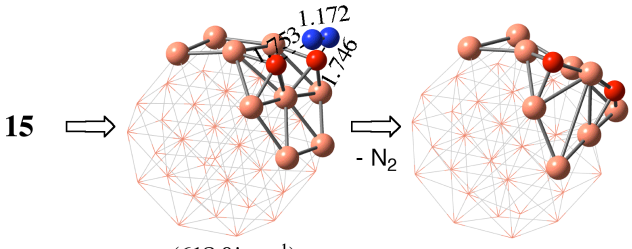

(618.0*i* cm^{-1})

$\mathbf{TS_{15\text{-}18}}$ (-29.1) **18** (-119.4)

Figure S4. Geometry changes of the N_2 formation from ONNO species adsorbed on Cu_{38}. In parentheses are the Gibbs energy change relative to Cu_{38} + 2 NO + CO. Distances and energies are in angstrom and kcal/mol, respectively.

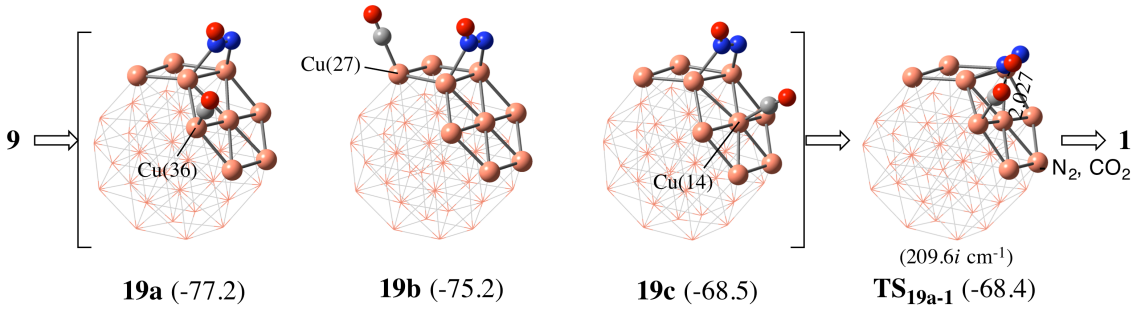

Figure S5. Geometry changes in N_2O-CO co-adsorption followed by O abstraction by CO on Cu_{38}. In parentheses are the Gibbs energy change relative to Cu_{38} + 2 NO + CO. Distances and energies are in angstrom and kcal/mol, respectively.

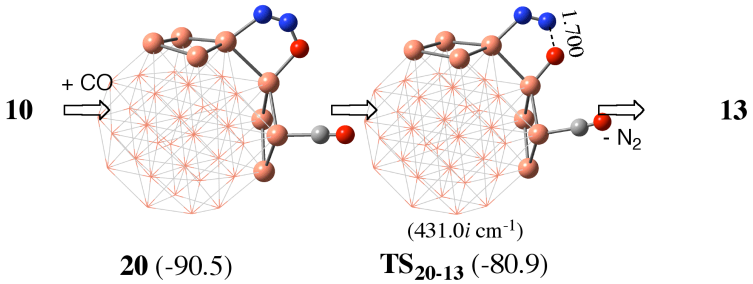

Figure S6. Geometry changes in N_2 formation from N_2O - CO co-adsorption structure (isomer of Figure S5) on Cu_{38}. In parentheses are the Gibbs energy change relative to Cu_{38} + 2 NO + CO. Distances and energies are in angstrom and kcal/mol, respectively.

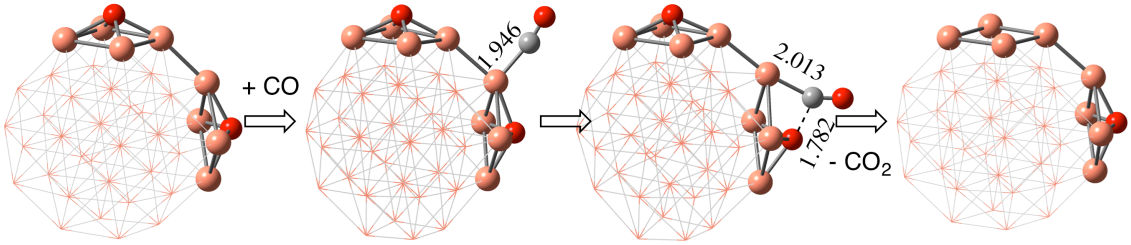

21 (0.0) **22** (-12.5) **TS$_{22\text{-}12}$** (-3.1) **12** (-37.5)

Figure S7. Geometry changes in CO_2 formation in the presence of another O -adsorption structure on Cu_{38}. In parentheses are the Gibbs energy change relative to the two O atom-adsorption structure **21**. Distances and energies are in angstrom and kcal/mol, respectively.

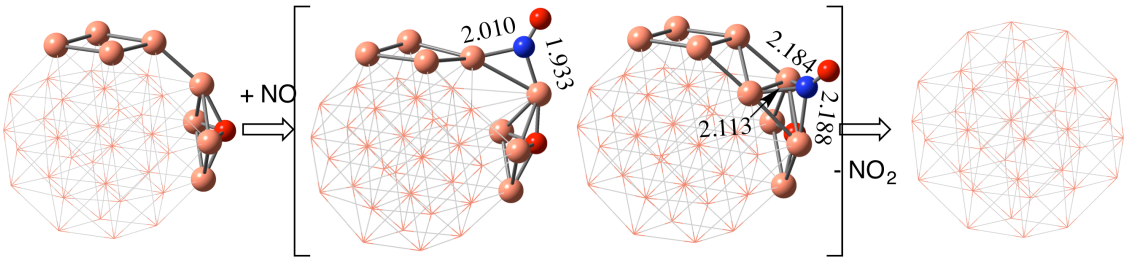

12 (-140.0) **23a** (-150.5) **23b** (-139.6) **1** (-111.5)

Figure S8. Geometry changes in N_2O formation from O -adsorption structure on Cu_{38}. In parentheses are the Gibbs energy change relative to Cu_{38} + 2 NO + CO. Distances and energies are in angstrom and kcal/mol, respectively.

4. CASSCF Calculations for NO Dimer

We investigated the electronic structures of free NO dimers and the ONNO species in **7**, using the CASSCF method, where the experimental geometry (the N-N distance, the N-O distance, and the O-N-N bond angle are 2.263 Å, 1.512 Å, and 97.2°, respectively)[S5] and that taken from **7** were employed for the free NO dimer. As shown in Figure S9a, the electron occupations of $\phi(N_2O_2\text{-}g)_{13}$ (1.78), $\phi(N_2O_2\text{-}g)_{14}$ (1.76), and $\phi(N_2O_2\text{-}g)_{15}$ (1.58) are significantly smaller than two. This feature leads to the weakening of the N-N bond because $\phi(N_2O_2\text{-}g)_{13}$ and $\phi(N_2O_2\text{-}g)_{15}$ contribute to the N-N bonding interaction. Instead, the occupation of $\phi(N_2O_2\text{-}g)_{16}$ (0.49), $\phi(N_2O_2\text{-}g)_{17}$ (0.24), and $\phi(N_2O_2\text{-}g)_{18}$ (0.22) are considerably larger than zero. Also, this feature leads to the weakening of the N-N bond because $\phi(N_2O_2\text{-}g)_{16}$ and $\phi(N_2O_2\text{-}g)_{18}$ contribute to the N-N anti-bonding interaction. As a result, the NO dimer has a long N-N distance and small N-N bond energy in the gas phase. In the NO dimer taken from **7**, as shown in Figure S9b, the multi-configuration character significantly decreases where the occupation number of $\phi(N_2O_2\text{-}\mathbf{7})_{13}$, $\phi(N_2O_2\text{-}\mathbf{7})_{14}$, and $\phi(N_2O_2\text{-}\mathbf{7})_{15}$ orbitals becomes close to 2; 1.96, 1.91, and 1.88, respectively.

Because **7** is too large to perform the CASSCF calculation, we investigated here a small model Cu_2-ONNO, where the ONNO moiety was optimized with the Cu-Cu distance fixed to 2.467 Å (the Cu-Cu distance in **7**); named **7M**. As shown in Table S5, the N-N, Cu-N, and N-O distances, the NBO charge, and the spin distributions of **7M** are similar to those of **7**, indicating that the geometry and electronic structure of **7** are reproduced well by **7M**. Then, the CASSCF calculation is performed for **7M**. The natural orbitals and the electron occupation number of **7M** at the CASSCF method are presented in Figure S9(c). In **7M**, it is shown that the charge transfer (CT) significantly occurs from the 4*s* orbitals of two Cu atoms ($\phi(\mathbf{7M})_{34}$) to the N-N bonding orbital of the

ONNO moiety (ϕ(**7M**)$_{35}$) about 1 *e*, where the ϕ(**7M**)$_{36}$ orbital corresponds to the vacant ϕ(N_2O_2-g)$_{17}$ and ϕ(N_2O_2-**7**)$_{16}$ orbitals in the isolated NO dimer (Figures S9a and S9b). This CT explains that the ONNO moiety has the shorter and stronger N-N bond both in **7** and **7M**. The NBO charge of **7** and **7M** also indicate that the CT significantly occurs from Cu to the ONNO moiety (Table S5). In other words, this CT accelerates the formation the ONNO structure and stabilizes it. In addition, the ϕ(**7M**)$_{35}$ orbital has an anti-bonding contribution of the N-O bond as shown in Figure S9(c). Thus, the CT form Cu to the ϕ(**7M**)$_{35}$ orbital also contributes to the N-O bond dissociation. This is the reason why the N-O bond is cleaved with such small activation energy on Cu_{38}.

It is also notable that the multi configuration character clearly disappears in **7M**, because the CT stabilizes the ϕ(**7M**)$_{35}$ orbital and destabilizes the ϕ(**7M**)$_{36}$ orbital, which breaks degeneracy of these orbitals. These results show that the electronic structure of the ONNO moiety on Cu_{38} can be described by the DFT method.

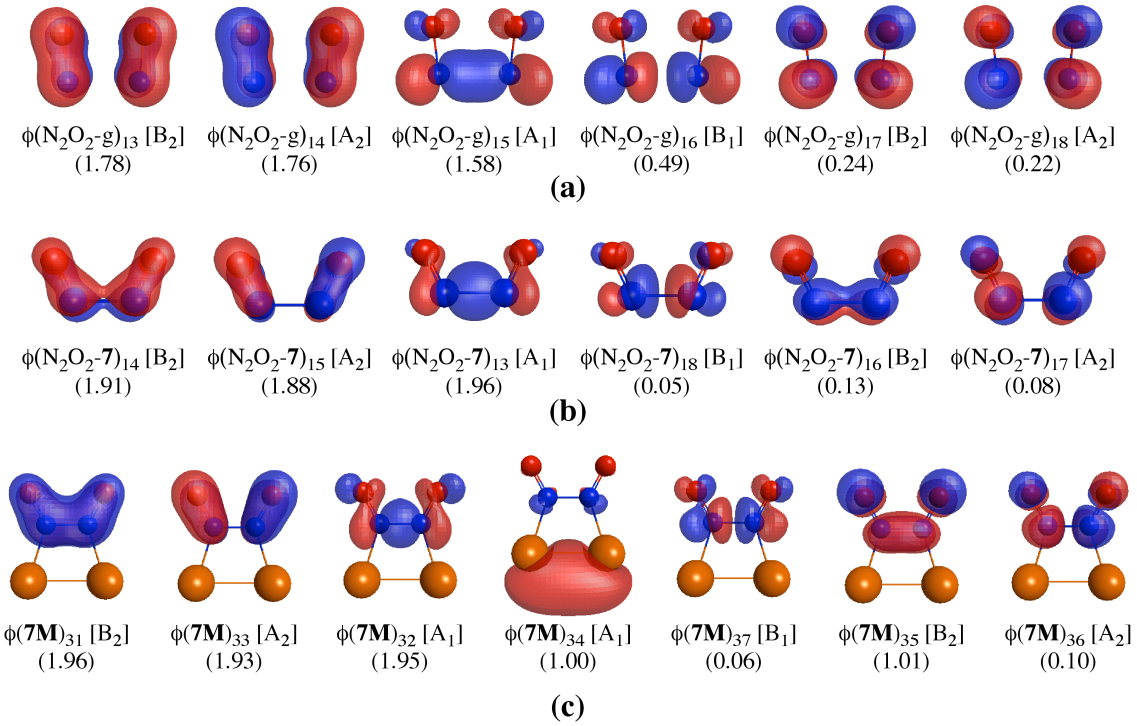

Figure S9. Representative natural orbitals and electron occupation numbers of (a) NO

dimer (ONNO) in the gas phase,[a)] (b) NO dimer taken from **7**,[b)] and (c) **7M**.

[a)] Calculated at the CASSCF(14e,12o)/cc-pVTZ method using the experimental geometry.

[b)] Calculated at the CASSCF(14e,12o)/cc-pVTZ method using the geometry taken from **7**.

[c)] Calculated at the CASSCF(16e,14o)/cc-pVTZ method using the geometry of **7M**.

5. Orbital Changes in Formation of ONNO Species on Cu_{38} and Oxidation of CO with O Atom Adsorbed on Cu_{38}

In formation of ONNO species on Cu_{38}, the highest energy occupied MO (ϕ_{HO}) localized on the Cu_{38} surface, which plays an important role in charge transfer to NO molecules from Cu_{38}, becomes lower in energy on going to **7** (−6.36 eV) from **6** (−5.96 eV) as shown in Figure S10.

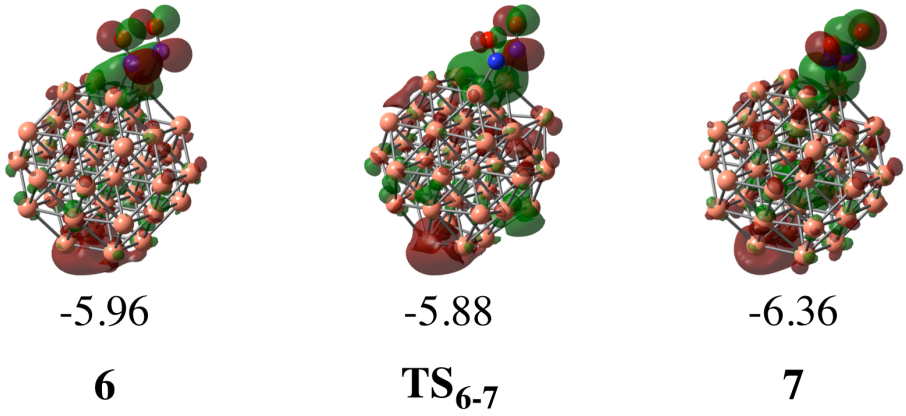

Figure S10. The highest energy occupied MO (ϕ_{HO}) localized on the Cu_{38} surface for NO dimerization. Energies are in eV.

In oxidation of CO with O atom adsorbed on Cu_{38}, the conversion of Cu_{38}-O **13** to Cu_{38} is a two-electron reduction reaction. Consistent with this understanding, the lowest energy unoccupied MO ϕ_{LU} of **13** becomes the highest energy occupied MO ϕ_{HO} in **1**, as shown in Figure S11.

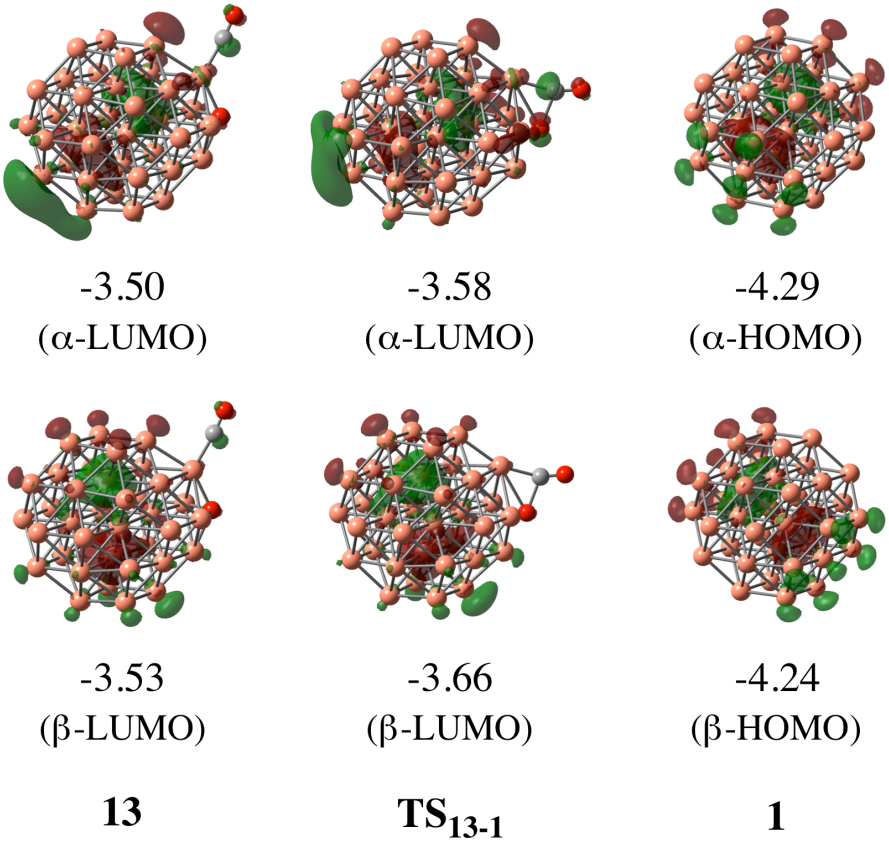

Figure S11. The lowest energy unoccupied MO (ϕ_{LU}) of **13** and **TS$_{13\text{-}1}$** and the highest energy occupied MO (ϕ_{HO}) of **1**. Energies are in eV.

6. Experimental Result for Cu Cluster Size

A quite weak diffraction peak due to Cu(111) was detected around 43.4° in the XRD pattern of 5 wt % Cu/γ-Al_2O_3 reduced at 773 K with 5 vol % H_2/He, as shown in Figure S12. This result indicates that Cu metal nanoparticles were highly dispersed on the γ-Al_2O_3 surface. The XRD pattern showed a very weak and broad diffraction peak around 2θ = 43-44°, which corresponds to the peak by the Cu particle, indicating that the diameter of the Cu cluster is less than 2 nm.

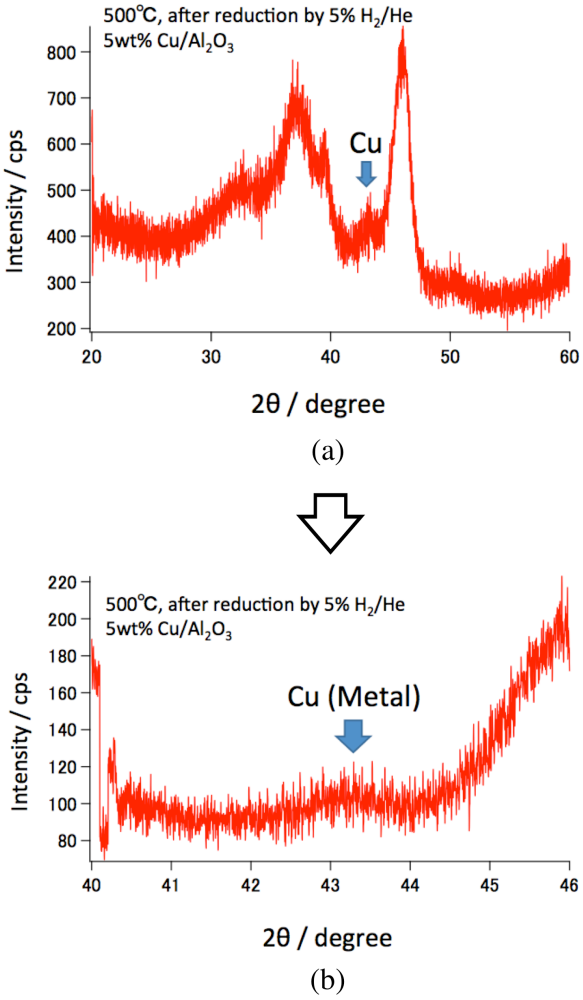

Figure S12. XRD pattern of 5wt % Cu/γ-Al_2O_3 after treated with 5 vol.% H_2/He at 773 K for 2θ from 20 to 60 degree (a) and 2θ from 40 to 46 degree (b).

X-ray powder diffraction (XRD) analyses were performed using Cu *K*α radiation (λ=1.5405 Å) and a one-dimensional X-ray detector (XRD: SmartLab, RIGAKU). The samples was scanned from 2Θ=20° to 60° at a scanning rate of 0.05 s^{-1} and a resolution of 0.005°. The Figure S9(a) shows that the apparent peak cannot be observed around 43 to 44°, indicating that the Cu particle larger than 2 nm is not involved in the catalyst. It is noted that CuO is not observed here, as well as the absence of XPS peak of Cu(II).

7. Change of NBO Charge for Oxidation of CO with O Atom adsorbed on Cu_{38}

In the CO reaction with the O atom adsorbed on Cu_{38}, the sum of electron populations of CO and O becomes moderately more negative at $\mathbf{TS_{13\text{-}1}}$ but then changes to zero in CO_2 at **1** + CO_2. Though the electron population of Cu_{38} moderately decreases at $\mathbf{TS_{13\text{-}1}}$, it finally increases at **1** + CO_2, as shown in Table S1.

Table S1. Change of the NBO charge for oxidation of CO with O atom adsorbed on Cu_{38}.

	13	$\mathbf{TS_{13\text{-}1}}$	**1**
q(O)	-1.196	-1.115	-0.522
q(CO)	+0.157	+0.028	+0.522
q(CO_2)	-1.039	-1.088	0.000
q(Cu_{38})	+1.039	+1.088	0.000

8. DFT Functional Dependency on Energetics

Though pure DFT functionals have been used in many theoretical studies of metal particle/cluster, it is likely that the use of the hybrid functional is better to investigate geometry and electronic structure of organic molecule and its reaction on metal cluster/particle. We calculated the energy change by using the PBE functional for the NO dimerization step (from **6** to **7**) and CO_2 formation step (from **13** to **1**). As shown in Table S2, the energetics at the B3LYP level is similar to those at the PBE level; the transition states are moderately underestimated about 2 kcal/mol for the NO dimerization and moderately overestimated the transition state and the product for the CO_2 formation by 2 – 4 kcal/mol. Thus, the B3LYP functional is not bad for description of the energetics for the NO-CO reaction on Cu_{38} cluster.

Table S2. Energy change (ΔE in kcal/mol) for NO dimerization (from **6** to **7**) and CO_2 formation (from **13** to **1**) on Cu_{38} cluster at the B3LYP and PBE functionals.

	6	**TS_{6-7}**	**7**	**13**	**TS_{13-1}**	**1**
B3LYP	0.0	+10.6	-13.3	0.0	+11.4	-11.5
PBE	0.0	+13.0	-13.0	0.0	+9.6	-7.3

9. Basis Set Superposition Error (BSSE) Correction

The BSSE correction shows that the error is evaluated about 4.8 ~ 5.0 kcal/mol for NO adsorption and 5.3 ~ 5.7 kcal/mol for CO adsorption, as shown in Table S3. The BSSE error is similar between CO and NO adsorption. After CO and NO adsorption, the energy change suffers little from BSSE correction. Therefore, the discussion and conclusion do not change by using these results with BSSE correction.

Table S3. Calculated basis set super position error (BSSE in kcal/mol) for NO and CO adsorption on Cu_{38}.

	NO adsorption		CO adsorption	
	2a	**2b**	**3a**	**3b**
BSSE	5.0	4.8	5.3	5.7

10. Spin Multiplicities and S^2 Eigenvalues

The spin multiplicities and the S^2 eigenvalues for the calculated species are summarized in Table S4. The results show that the spin contamination is small for all the species.

Table S4. Spin multiplicity and the S^2 eigenvalues for the typical calculated species.

	1	**2a**	**2b**	**3a**	**3b**	**4a**	**4b**
spin	triplet	doublet	quartet	singlet	singlet	doublet	triplet
s^2	2.007	0.771	3.769	0.000	0.000	0.764	1.938
	6	**7**	**8a**	**9**	**10**	**11**	**12**
spin	triplet	triplet	triplet	triplet	triplet	triplet	triplet
s^2	2.029	2.040	2.020	2.254	2.580	2.007	2.006
	13						
spin	triplet						
s^2	2.008						

11. Geometrical Parameters, NBO Charge, and Electron Spin Distribution of 7 and 7M

As shown in Table S5, the N-N, Cu-N, and N-O distances, the NBO charge, and the spin distributions of **7M** are similar to those of **7**, indicating that the geometry and electronic structure of **7** are reproduced well by **7M**. Then, the CASSCF calculation is performed for **7M**.

Table S5. Geometrical parameters, NBO charge, and electron spin distribution of **7** and **7M**.

	7	**7M**
R(Cu-Cu)	2.647	2.647[a)]
R(N-N)	1.443	1.448
R(Cu-N)	2.054	2.032
R(N-O)	1.223	1.228
q[N] / spin	+0.04 / 0.10	-0.03 / 0.18
q[O] / spin	-0.28 / 0.38	-0.28 / 0.43

[a)] The Cu-Cu distance is fixed at that in **7**.

12. Complete Reference of Ref. 49

49 Gaussian 09, Revision D.01,

Frisch, M. J.; Trucks, G. W.; Schlegel, H. B.; Scuseria, G. E.; Robb, M. A.; Cheeseman, J. R.; Scalmani, G.; Barone, V.; Mennucci, B.; Petersson, G. A.; Nakatsuji, H.; Caricato, M.; Li, X.; Hratchian, H. P.; Izmaylov, A. F.; Bloino, J.; Zheng, G.; Sonnenberg, J. L.; Hada, M.; Ehara, M.; Toyota, K.; Fukuda, R.; Hasegawa, J.; Ishida, M.; Nakajima, T.; Honda, Y.; Kitao, O.; Nakai, H.; Vreven, T.; Montgomery, Jr., J. A.; , Peralta, J. E.; Ogliaro, F.; Bearpark, M.; Heyd, J. J.; Brothers, E.; Kudin, K. N.; Staroverov, V. N.; Keith, T.; Kobayashi, R.; Normand, J.; Raghavachari, K.; Rendell, A.; Burant, J. C.; Iyengar, S. S.; Tomasi, J.; Cossi, M.; Rega, N.; Millam, J. M.; Klene, M.; Knox, J. E.; Cross, J. B.; Bakken, V.; Adamo, C.; Jaramillo, J.; Gomperts, R.; Stratmann, R. E.; Yazyev, O.; Austin, A. J.; Cammi, R.; Pomelli, C.; Ochterski, J. W.; Martin, R. L.; Morokuma, K.; Zakrzewski, V. G.; Voth, G. A.; Salvador, P.; Dannenberg, J. J.; Dapprich, S.; Daniels, A. D.; Farkas, O.; Foresman, J. B.; Ortiz, J. V.; Cioslowski, J.; Fox, D. J. Gaussian, Inc., Wallingford CT, 2013.

REFERENCE

(S1) Perdew, J. P.; Burke, K.; Ernzerhof, M. Generalized Gradient Approximation Made Simple. *Phys. Rev. Lett.* **1996**, *77*, 3865-3868.

(S2) Kresse, G.; Hafner, J. *Ab initio* molecular dynamics for liquid metals. *Phys. Rev. B: Condens. Matter Mater. Phys.* **1993**, *47*, 558 - 561.

(S3) Kresse, G.; Hafner, J. *Ab initio* molecular-dynamics simulation of the liquid-metal-amorphous-semiconductor transition in germanium. *Phys. Rev. B: Condens. Matter Mater. Phys.* **1994**, *49*, 14251 - 14269.

(S4) Kresse, G.; Joubert, D. From ultrasoft pseudopotentials to the projector augmented-wave method. *Phys. Rev. B: Condens. Matter Mater. Phys.* **1999**, *59*, 1758 - 1775.

(S5) Fajín, J. L. C.; Cordeiro, M. N. D. S.; Gomes, J. R. B. Unraveling the mechanism of the NO reduction by CO on gold based catalysts. *J. Catal.* **2012**, *289*, 11 – 20.